Journal of Physics: Condensed Matter

PAPER

Lattice dynamics of $BaFe_2Se_3$

To cite this article: M J Weseloh *et al* 2022 *J. Phys.: Condens. Matter* **34** 255402

IOP Publishing Journal of Physics: Condensed Matter

J. Phys.: Condens. Matter **34** (2022) 255402 (13pp) https://doi.org/10.1088/1361-648X/ac640d

Lattice dynamics of $BaFe_2Se_3$

M J Weseloh[1,2], **V Balédent**[3], **W Zheng**[3], **M Verseils**[4], **P Roy**[4],
J B Brubach[4], **D Colson**[5], **A Forget**[5], **P Foury-Leylekian**[3]
and M-B Lepetit[1,2,*]

[1] Institut Néel, CNRS, Université Grenoble Alpes, 25 av. des Martyrs, 38042 Grenoble, France
[2] Institut Laue-Langevin, 71 av. des Martyrs, 38000 Grenoble, France
[3] CNRS, Laboratoire de Physique des Solides, Université Paris-Saclay, 91405, Orsay, France
[4] Synchrotron SOLEIL, L'Orme des Merisiers, Saint Aubin BP 48, 91192, Gif-sur-Yvette, France
[5] SPEC, CEA, CNRS-UMR3680, Université Paris-Saclay, Gif-sur-Yvette Cedex 91191, France

E-mail: Maria.Weseloh@neel.cnrs.fr and Marie-Bernadette.Lepetit@neel.cnrs.fr

Received 20 January 2022, revised 21 March 2022
Accepted for publication 4 April 2022
Published 6 May 2022

Abstract

This paper presents a study of the lattice dynamics in $BaFe_2Se_3$. We combined first-principle calculations, infrared measurements and a thorough symmetry analysis. Our study confirms that *Pnma* cannot be the space group of $BaFe_2Se_3$, even at room temperature. The phonons assignment requires *Pm* to be the $BaFe_2Se_3$ space group, not only in the magnetic phase, but also in the paramagnetic phase at room temperature. This is due to a strong coupling between a short-range spin-order along the ladders, and the lattice degrees of freedom associated with the Fe–Fe bond length. This coupling induces a change in the bond-length pattern from an alternated trapezoidal one (as in *Pnma*) to an alternated small/large rectangular one. Out of the two patterns, only the latter is fully compatible with the observed block-type magnetic structure. Finally, we propose a complete symmetry analysis of the $BaFe_2Se_3$ phase diagram in the 0–600 K range.

Keywords: phonons, symmetry, multiferroics, DFT, IR

S Supplementary material for this article is available online

(Some figures may appear in colour only in the online journal)

1. Introduction

Strong quantum entanglement of electron wave-functions, also called strong electronic correlation, is at the origin of many remarkable properties. This is the case, for instance, with superconductivity, colossal magneto-resistance, or magneto-electric (ME) coupling. Since electronic correlations are intrinsic quantum mechanical effects, the related properties are primarily expected at low temperatures. However, a few families of compounds exhibit exceptionally high working temperatures. An example is given by the cuprates family [1] with its record superconducting transition temperature of 164 K under 45 GPa pressure [2], and 133 K at ambient pressure [3]. Another family, in which high-temperature superconductivity was found, is the iron-based pnictides family [4]. In this family the inherent multi-orbital character adds a lot of complexity, therefore, iron-based pnictides have been the subject of numerous studies since their discovery in 2006 [5]. In addition to their superconducting properties, some of the pnictides exhibit multiferroic properties [6] (a state with at least two coexisting/coupled ferroic/antiferroic orders), thus increasing their interest for the community.

In the last decade, a lot of research effort has been devoted to multiferroicity, and more specifically to ME multiferroics. Due to the coupled nature of their electrical and magnetic orders, ME compounds offer the possibility to control their magnetic properties by applying a simple voltage, or control their polarization or dielectric constant by applying a mag-

---

[*] Author to whom any correspondence should be addressed.

netic field. Hence, they are highly promising for new kinds of electronic devices.

Among the ME compounds, $BaFe_2Se_3$ is one of the few materials exhibiting both a magnetic order and a polarization at high temperatures. Indeed, below the Néel temperature (T_N is reported between 200 K and 256 K according to the authors) a long-range block-type antiferromagnetic (AFM) ordering sets in [7–11]. Gao *et al* have attributed the large range found for T_N to different stoichiometric ratios in grown crystals [11]. Additionally to the large T_N, $BaFe_2Se_3$ shows quasi-one-dimensional superconductivity under pressure [12].

X-ray experiments first proposed the non-polar space group *Pnma* [8] for $BaFe_2Se_3$. A few years later, Dong *et al* [13] theoretically predicted that the observed block-type magnetic order should induce a polar symmetry lowering, due to exchange-striction effects. Weak intensity was later observed on the $hk0$, $h = 2n + 1$ peaks of the x-ray diffraction pattern, that are forbidden in the *Pnma* group [14]. Instead of *Pmna*, the polar space group $Pmn2_1$ was proposed for $BaFe_2Se_3$ room temperature structure [14]. Below T_N, a further symmetry lowering was observed and assigned to a transition from $Pmn2_1$ to *Pm* [14].

The $BaFe_2Se_3$ compound presents a quasi-one-dimensional ladder geometry coherent with its superconducting properties (see figure 1). The iron atoms are in a $FeSe_4$ tetrahedral environment. These edge-sharing tetrahedra form two-legs ladders along the $\vec{b}$ direction (standard *Pnma* setting). Each unit cell contains two ladders (one at the center and one at the corners of the unit cell) separated by barium atoms. In each unit cell, there are two Fe atoms per chain along the ladder direction, and thus two types of Fe–Fe bonds: one within the unit cell and one between cells. While in the *Pnma* group there is only one independent Fe site, in $Pmn2_1$, the two chains in a ladder are associated to independent Fe sites, whilst the two ladders in the unit cell remain symmetry related. This remaining symmetry is however lifted at the magnetic-ordering transition with the $Pmn2_1$ to *Pm* symmetry lowering. Another important difference between the *Pnma*, and $Pmn2_1$ or *Pm* structures, is the Fe–Fe bond alternation along the ladder direction. Whereas the *Pnma* space-group symmetry imposes that a long bond faces a short one along the ladders—thus building alternated trapezoidal blocks along the ladder direction—in the lower symmetry groups, this constraint is lifted and the $Pmn2_1/Pm$ structures [14] posses long (short) bonds that are at the same level along the ladder direction (see figure 6). The latter geometry is in good agreement with the block magnetic order seen in neutron scattering measurements [8, 15]. In this respect, $BaFe_2Se_3$ is different from most multiferroics. Prominent is that $BaFe_2Se_3$ is rather ferrielectric than ferroelectric, with a strong polarization in each ladder, mostly canceling out between the ladders. Its fully ferroelectric state has an energy predicted only slightly higher than the ferrielectric one; the latter holds a giant improper polarization predicted to be $\sim 2-3\ \mu C\ cm^{-2}$, while the ferrielectric one was predicted to be $\sim 0.2\ \mu C\ cm^{-2}$ [13] and experimentally estimated around $\sim 0.6\ \mu C\ cm^{-2}$ [16].

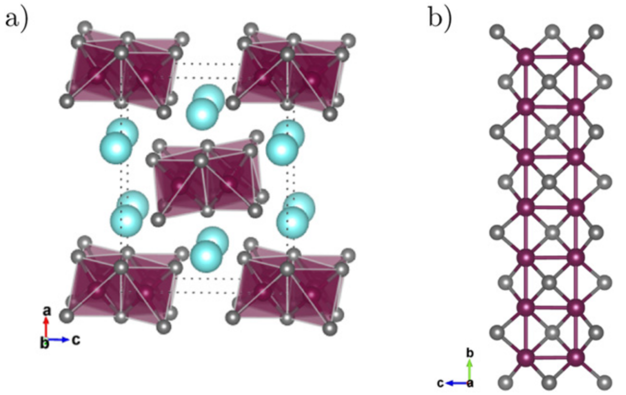

Figure 1. General structure of $BaFe_2Se_3$ illustrated from the *Pnma* data. The Fe atoms and Fe–Se tetrahedra are shown in purple, the Se atoms are shown in gray, and the barium atoms are shown in light-blue. (a) Crystal structure of $BaFe_2Se_3$. (b) Structure of the Fe-ladders.

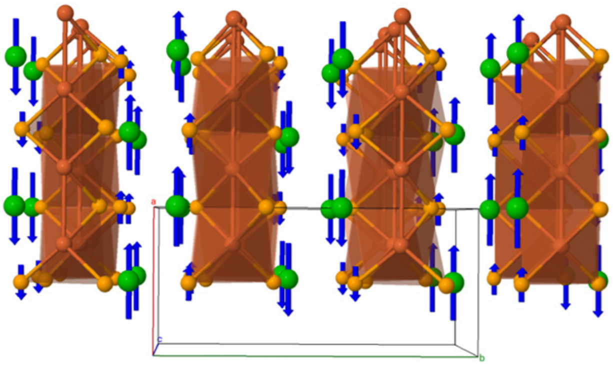

Figure 2. Schematic representation of the displacement vector associated with the phonon mode measured at 61 cm^{-1} and computed at 60 cm^{-1}. It is to be noted that the inter-ladder spin ordering was not taken into account in our calculations.

In this paper we present a lattice-dynamic study, combining experimental infrared (IR) spectroscopy studies with first principle density-functional theory (DFT) calculations. It is well known that phonon spectra are of crucial importance in multiferroic systems. In particular, they are often much more efficient than diffraction methods to reveal weak symmetry breaking and to distinguish between space groups.

The next section will detail both experimental and numerical methods. Section 3 will be devoted to the IR measurements, and section 4 to DFT results and discussion.

2. Methods

2.1. Experimental

The experimental phonon modes were measured on two pieces of the high quality single-crystals of reference [14]. In these crystals, neutron diffraction measurements yielded a Néel temperature close to 200 K [14]. We fixed them with silver paint on a copper sample holder to ensure a good thermal conductivity. Both samples were carefully aligned to put the electric and magnetic fields of the incident beam

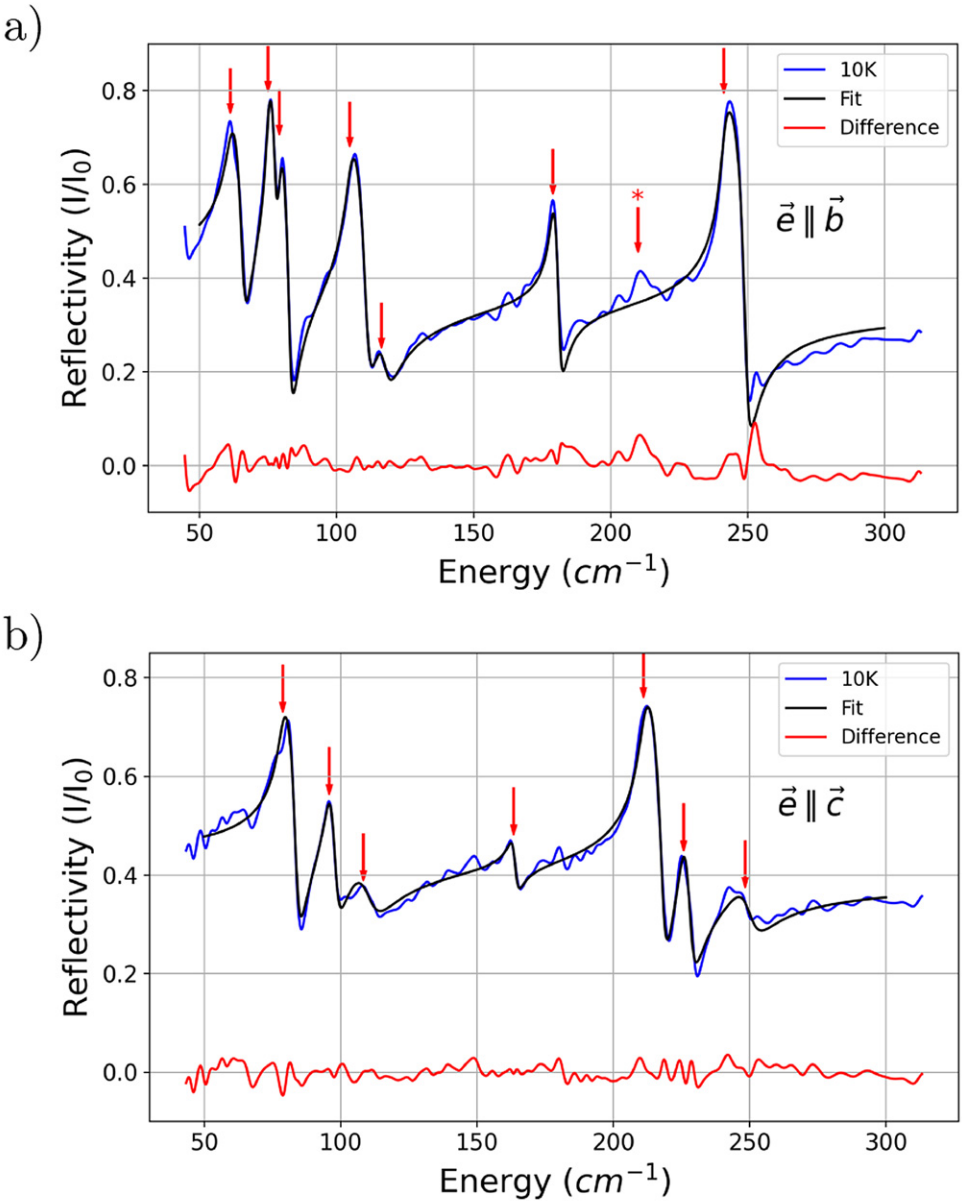

Figure 3. Infrared measurements at 10 K. Axes defined in the *Pnma* standard setting, (a) the electric field is along the $\vec{b}$ direction, (b) the electric field is along the $\vec{c}$ direction. Red arrows points the phonons positions ω_k, stars indicate phonon positions not successfully fitted.

(labeled (e) and (h)), in the ($\vec{c}, \vec{b}$) and ($\vec{b}, \vec{c}$) crystallographic directions.

Infrared spectroscopy measurements were carried out on the AILES beamline of the SOLEIL synchrotron, with a Bruker IFS125 Michelson interferometer [17] equipped with a closed circle He-gas cryostat, a 4.2 K bolometer, and a 6 μm beam splitter for a resolution of 2 cm^{-1}. The synchrotron radiation beam was linearly polarized thanks to polyethylene polarizers. For each crystal, the reflectivity was recorded for several temperatures from 10 to 300 K. The absolute reflectivity of the sample was obtained by using as reference the same gold-coated sample obtained by *in situ* gold coating evaporation technique. As a consequence, each reflectivity spectra is the ratio between the reflected intensity on the sample and the reflectivity from the gold deposited on the sample surface.

2.2. Theoretical

The phonon modes were calculated using DFT, after a full geometry optimization within the constraints of a given space group. We used the CRYSTAL code [18, 19]. This code has the advantage that the whole vol A of the crystallographic tables [20] has been coded in it. CRYSTAL is therefore one of the most convenient DFT code for symmetry analyses as it can decipher the phonons spectra issued from different space groups. This code also offers the advantage to use atomic Gaussian basis sets and hence enables the use of hybrid functionals with nearly no additional computational costs. Since our system is strongly correlated and presents metallic, semiconducting and magnetically ordered phases [7], it is important to use a hybrid functional in order to describe at the best the system's electronic structure. For this purpose we use the B3LYP functional [21, 22].

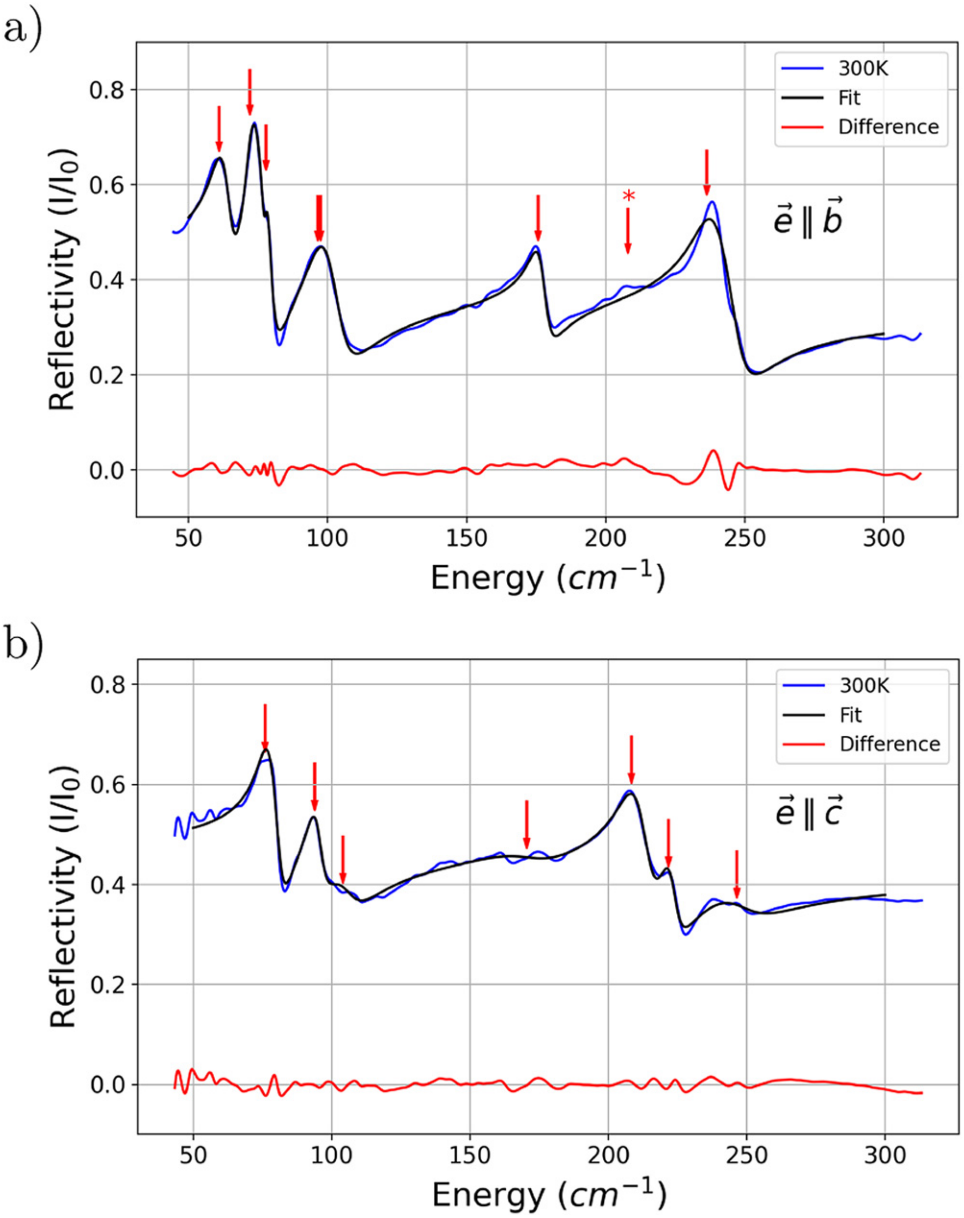

Figure 4. Infrared measurements at 300 K. Axes in the *Pnma* standard setting, (a) the electric field is along the $\vec{b}$ direction, (b) the electric field is along the $\vec{c}$ direction. Red arrows point the phonons positions ω_k, stars indicate the phonon positions not successfully fitted.

The atomic basis sets were chosen as all-electrons, valence $3\zeta + \mathrm{p}$ basis set for the Fe and Se atoms [23], a relativistic core pseudo-potential of the Stuttgart group [24] for the Ba atom, and the associated basis set adapted to solid-state calculations [23]. Since the unit cell does not change in the different groups, we used a $5 \times 10 \times 6$ Monkhorst–Pack **k**-grids (*Pnma* axes) for all calculations in the single unit cell, and an equivalent grid spacing for the calculations in the double unit cell.

The phonon modes were computed at the center of the Brillouin zone using the harmonic approximation. We performed two types of calculations: calculations without spin polarization within a single unit cell, and calculations with spin polarization along the chains—$(0, \frac{1}{2}, 0)$ propagation vector in the *Pnma* axes—within a double unit cell. The experimental propagation vector is $(\frac{1}{2}, \frac{1}{2}, \frac{1}{2})$ [8, 15]. Hence, to completely account for the magnetic order the calculation should be done in a $2a \times 2b \times 2c$ supercell. Unfortunately, such a unit cell is too large for performing geometry optimization and phonons calculations with our current computer resources. We thus opted for a feasible compromise that sets properly the magnetic order within the ladders, as it is associated with the largest magnetic integrals of the system.

3. Infrared measurements

The reflectivity measurements of $\mathrm{BaFe_2Se_3}$ between 10 K and 300 K were performed at quasi-normal incidence, with the electric field along the *b*-axis and *c*-axis in the *Pnma* standard setting. Figure 3(a) and (b) displays the same IR measurements at 10 K for these two configurations. As we can see, eight phonons modes are visible when the field is along

Table 1. Fitted phonons frequencies (cm^{-1})—for both polarization configurations $e//\vec{b}$ and $e//\vec{c}$—from the IR reflectivity spectra shown in figures 3 and 4. The position at 300 K of the 116 cm^{-1} ($e//\vec{b}$) and 161 cm^{-1}($e//\vec{c}$) phonons could not be determined within an acceptable error-bar, due to the loss of intensity and dampening. Systematic error bars are estimated smaller than 3 cm^{-1}. Stars indicate that the value is estimated graphically with an error of 6 cm^{-1}.

$e//\vec{b}$		$e//\vec{c}$	
10 K	300 K	10 K	300 K
61	60	79	76
75	72	96	94
79	78	108	104
105	97	163	—
116	—	211	208
179	176	226	222
210*	207*	248	246
241	236		

$\vec{b}$ and seven when the field is along $\vec{c}$. The number of observed modes is unchanged between 300 K (see figure 4) and 10 K, despite a large broadening at high temperature, making some phonons difficult to accurately fit. Experimental phonons frequencies were obtained by fitting the data using the usual Drude–Lorentz model for the dielectric function of insulating materials. The dielectric function is thus expressed as the sum of harmonic oscillators:

$$\epsilon(\omega) = \epsilon_\infty + \sum_k \frac{A_k \omega_k^2}{\omega_k^2 - \omega^2 - i\Gamma_k \omega} \qquad (1)$$

where ϵ_∞ is the dielectric constant at infinite frequency, ω_k, A_k and Γ_k the resonant frequency, the amplitude and energy-width of the kth harmonic oscillator. The resulting phonon frequencies are reported for both extreme temperatures (10 K and 300 K) in table 1, in order to compare them to DFT results. The typical errors for the phonon energies, combining experimental resolution and fit, are estimated to be smaller than 3 cm^{-1}.

The temperature dependence of the three parameters, ω_k, A_k and Γ_k are represented for both polarization configurations in figure 5. Some of the phonons are too dampened and/or not enough intense to accurately follow their position, width and amplitude as function of temperature. This is the case for the modes at 161 cm^{-1} ($e//\vec{c}$) and 116 cm^{-1}($e//\vec{b}$). From the evolution of their energies, we can see that all phonons undergo a hardening with decreasing temperature. More interesting, we can observe a quasi-systematic anomaly around the Néel temperature at 200 K. For example, nearly all phonons measured for $e//\vec{b}$ display a drop in amplitude, A_k, around 200 K, concomitant to a change in the linewidth evolution.

A kink in the energy, ω_k, is also observed at the same temperature for the 61 cm^{-1} phonon, but without any effect on its amplitude. This can be easily explained by the experimental limitations. Indeed, the limited number of data points at low energies makes it difficult to determine a baseline, thus affecting the fit of the amplitude and width of the mode, without impacting the phonon position. Figure 2 shows a schematic representation the displacement vector associated with this phonon mode as obtained in the DFT calculations. One sees immediately that it is mainly a displacement mode of the barium atoms along the ladders direction. This is associated with a displacement of one-out-of-two of the selenium atoms located on the outer part of the ladders. The Se displacements are also along the ladder direction but of weaker amplitude. As the pronounced renormalization of this mode occurs at the magnetic ordering temperature, we can related it to a spin-lattice interaction. The atomic displacements should however little affect the intra-ladder interactions, as neither the Fe atoms, not the Se atoms bridging the Fe–Fe magnetic interaction are involved. The only expected effect on the intra-ladder interactions is the modification of the electrostatic potential seen by the ladders. These atomic displacements should however strongly interact with the inter-ladders interactions; fist because the latter are mediated by the displaced Se atoms, second because the Ba atoms are located between the ladders, on the interaction paths responsible for the 3D ordering.

For $e//\vec{c}$, mainly two phonons display an anomaly at 200 K, namely the modes at 211 cm^{-1} and 248 cm^{-1}. This anomaly can be seen in the three parameters ω_k, A_k and Γ_k.

All these observations strongly suggest a significant spin-phonon coupling in $BaFe_2Se_3$.

4. DFT calculations and discussion

We first fully optimized the structure, then computed the phonons spectra without spin polarization. Indeed, it is usually believed that in most systems spin ordering induce only small shifts (a few cm^{-1}) in the phonons frequencies. The calculations were performed in the *Pnma*, $Pmn2_1$ and *Pm* groups. The optimized geometries can be found in the supplementary material (https://stacks.iop.org/JPCM/34/255402/mmedia). All three calculations yielded similar energies, within DFT error-bars. Thus, one cannot discriminate between them on this criterium. All optimized geometries agree well with the experimental single crystal x-ray diffraction of reference [8]. The comparison (using the amplimode code [25, 26]) of the *Pnma*, $Pmn2_1$ and *Pm* calculations, with the room temperature experimental geometry of reference [8], yields similar degrees of lattice distortion (0.0027) for the three structures and measures of compatibility (0.028 for *Pnma* and *Pm* and 0.064 for $Pmn2_1$).

4.1. Symmetry analysis

69 optical phonon modes and three acoustic ones are expected at the Γ point. Symmetry analysis indicates that the IR phonons observed with the field along the $\vec{b}$ direction should belong to the B_{3u} irreducible representation (irrep) in the *Pnma* group, and to the B_{1u} irrep when the field is set along the $\vec{c}$ direction (see character tables in the supplementary material).

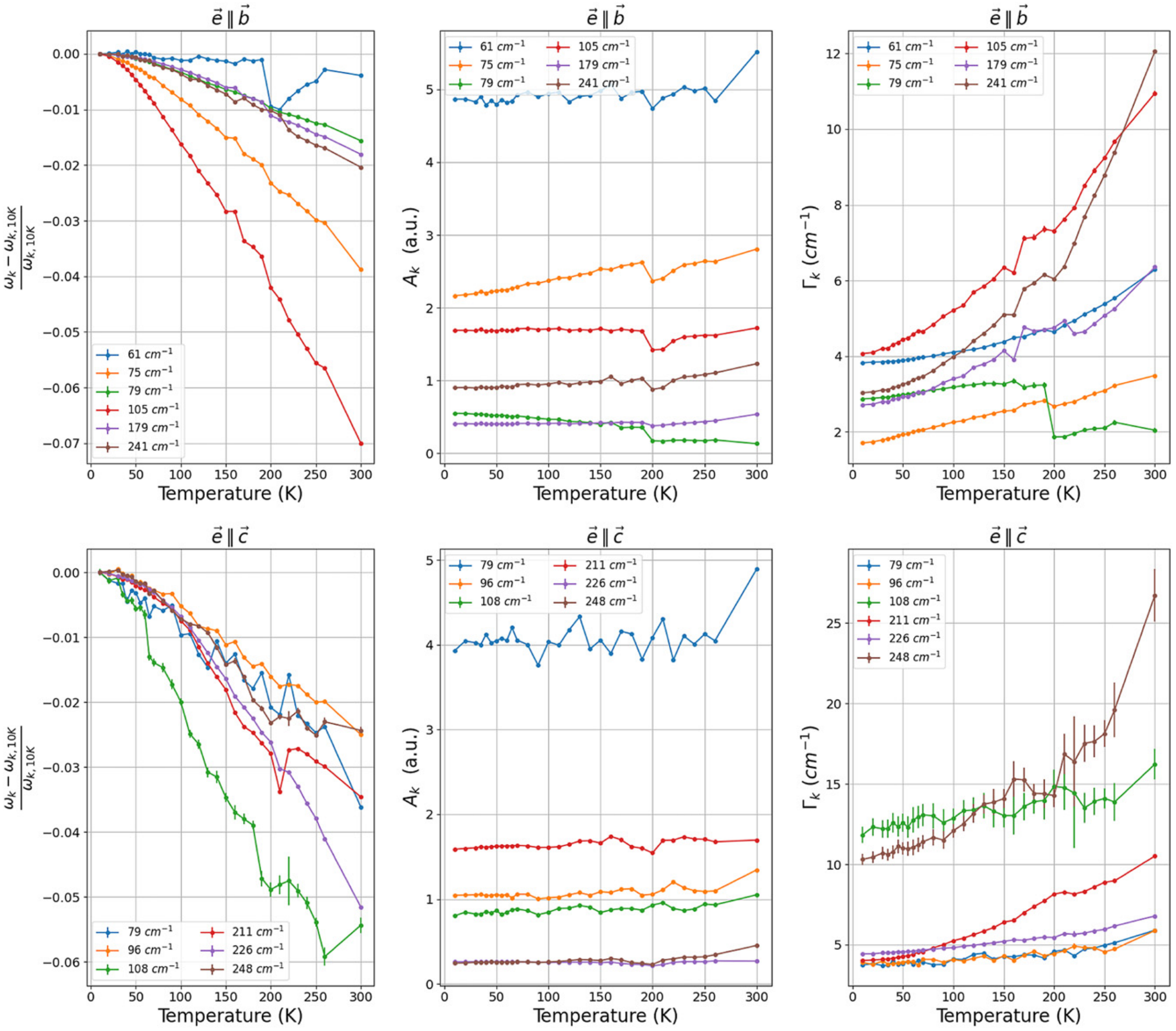

Figure 5. Temperature dependence of relative variation, with respect to low temperature, of ω_k, A_k and Γ_k. $e//\vec{b}$: top panels, $e//\vec{c}$: bottoms panels. When no error bars are visible, they are within the marker size.

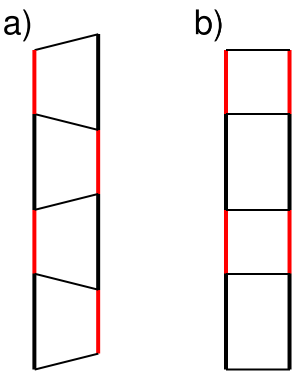

Figure 6. Illustration of the Fe–Fe bond lengths alternation along the ladders. (a) As encountered in the *Pnma* group and the non-spin polarized geometry optimizations within the $Pmn2_1$ and *Pm* groups. (b) As obtained from geometry optimizations taking into account spin-ordering along the ladders, within $Pmn2_1$ and *Pm* groups.

Table 2. Group/subgroup relationships between the irreducible representations of the *Pnma*, $Pmn2_1$ and *Pm* groups, and assignment of the different IR modes according to the electric field polarizations (axes defined as in *Pnma* standard setting).

e	*Pnma*		$Pmn2_1$	*Pm*
	A_g	Γ_1^+	A_1 Γ_1	A Γ_1
$e//\vec{c}$	B_{1u}	Γ_3^-		
	B_{3g}	Γ_2^+	B_1 Γ_4	
$e//\vec{a}$	B_{2u}	Γ_4^-		
	B_{1g}	Γ_3^+	A_2 Γ_3	B Γ_2
	A_u	Γ_1^-		
	B_{2g}	Γ_4^+	B_2 Γ_2	
$e//\vec{b}$	B_{3u}	Γ_2^-		

The group/subgroup relationships between the different irreps of the *Pnma*, $Pmn2_1$ and *Pm* groups are reported on table 2. They will be further used for the phonons assignments.

Table 3. Computed phonon modes in the $Pmn2_1$ group and their best assignment to the measured Raman and IR modes (cm^{-1}) at 300 K. The DFT calculations were carried out without spin polarization. The Raman modes were taken from reference [9] and the IR modes from our measurements.

DFT Irrep	$Pmn2_1$	Raman [9]	IR 300 K	
	ν	300 K	$e//\mathbf{b}$	$e//\mathbf{c}$
B_1	29.9			
A_1	33.4			
A_2	36.5			
A_1	39.5			
B_1	45.7			
B_1	51.5			
A_1	52.7			
B_1	60.2			
B_2	63.7		60	
A_1	64.4	59.0		
A_2	64.4			
A_1	66.6			
A_1	67.8			76
A_2	67.9			
B_1	70.8			
B_2	76.1		72	
B_1	79.5			
A_2	84.1			
B_1	86.4			
A_1	87.1	88.0		
B_2	89.1		78	
A_1	91.9			94
B_1	93.1			
B_2	101.1		97	
A_2	101.9			
A_2	112.2			
B_2	112.7		—	
A_1	113.2	104.3		104
A_1	114.7	111.0		
B_1	115.4			
B_1	117.4			
A_1	128.4	137.0		
B_2	133.4			
A_2	134.3			
B_1	135.2			
A_1	150.1			
B_1	156.2			
A_1	160.5			
B_1	163.2			
A_1	170.4			—
B_1	174.3			
B_2	184.1	177	176	
A_2	184.5			
B_1	186.2			
B_2	190.9			
A_2	192.3			
A_1	195.3	195.6		
A_2	224.5			
B_2	225.0	222.8		
A_1	250.1			246
B_1	251.5			
A_2	253.0			
B_2	253.2			
A_1	256.3	267		

(*continued on next page*)

Table 3. Continued

DFT Irrep	$Pmn2_1$	Raman [9]	IR 300 K	
	ν	300 K	$e//\mathbf{b}$	$e//\mathbf{c}$
B_1	260.9			
B_2	260.9			
A_2	261.9			
B_2	267.7			
A_2	267.8			
A_2	282.0			
B_2	282.5			
A_1	295.0	280.0		
A_1	295.5	290.0		
B_1	296.0			
B_1	298.0			
B_1	312.7			
A_1	314.8			
A_1	321.2			
B_1	325.6			

4.2. The Pnma space group

Out of the 69 optical phonon modes in the *Pnma* group, 36 modes are Raman active, 26 modes are IR active. The irrep distribution is as follows

$$\overbrace{11\,A_g \oplus 7\,B_{1g} \oplus 7\,B_{2g} \oplus 11\,B_{3g}}^{\text{Ramanactive}} \oplus \overbrace{10\,B_{1u} \oplus 10\,B_{2u} \oplus 6\,B_{3u}}^{\text{IRactive}} \oplus \overbrace{7\,A_u}^{\text{Inactive}}$$

The tables of the computed *Pnma* phonons modes can be found in the supplementary material.

In this group, the number of measured modes exceeds the number of predicted ones for different irreps. Seven modes were indeed measured in the B_{3u} irrep at 300 K (eight at 10 K), while only six are predicted by the symmetry analysis. In addition, some of the modes cannot be assigned because no calculated modes are available in the corresponding energy range. In total, there are two A_g, three B_{3u}, two B_{1u} and one B_{2g} modes that cannot be assigned within the *Pnma* group. Hence, in agreement with our previous x-ray diffraction work [14], the lattice dynamics clearly excludes the *Pnma* group, even in the paramagnetic phase.

4.3. The $Pmn2_1$ space group

Out of the 69 optical phonon modes expected in the $Pmn2_1$ group, all are Raman active and 55 IR active. Their distribution into the group's irreps is the following

$$\overbrace{\underbrace{21\,A_1 \oplus 21\,B_1 \oplus 13\,B_2}_{\text{IR active}} \oplus 14\,A_2}^{\text{Raman active}}$$

Tables 3 and 4 display the $Pmn2_1$ computed phonons modes and their best assignment to the measured modes. The IR modes stem from our measurements at 300 K, while the experimental Raman modes are taken from reference [9] at 300 K.

One sees immediately that all Raman modes can be assigned with a good accuracy in the $Pmn2_1$ group, with an average error of $\simeq$6 cm^{-1}. For the IR modes two modes are problematic along each direction.

Table 4. Measured (300 K) IR phonon modes (cm^{-1}) that could not be assigned to computed ones in the $Pmn2_1$ space group.

Irrep	Raman [9]	IR 300 K	
	300 K	$e//\mathbf{b}$	$e//\mathbf{c}$
A_1			208
A_1			222
B_2		207*	
B_2		236	

Along the $\vec{b}$ direction, the modes at 207 cm^{-1} and 236 cm^{-1} can only be assigned to the computed modes with quite large error bars (namely 18 cm^{-1} and 17 cm^{-1}). Such error bars are at the extreme limit of DFT acceptable error bars, and should attract our attention. In addition, the mode at 207 cm^{-1} has to be assigned to the same computed mode as the mode seen in Raman scattering at 222.8 cm^{-1}, which is nearly 16 cm^{-1} away. Even if one accept the large differences between the computed and experimental IR frequencies, the difference between the Raman and IR measurements seems too large to be accounted for by experimental error bars.

Nevertheless, the main problem occurs for IR modes when the electric field is set along the $\vec{c}$ direction. Indeed, the two most intense modes (see figure 4(b)), at 208 cm^{-1} and 222 cm^{-1} are impossible to assign as there are not any A_1 modes in the range 195–250 cm^{-1}. Even if the mode at 208 cm^{-1} was assigned to the computed mode at 195 cm^{-1}, with an error of 23 cm^{-1}, this mode was already assigned to a Raman mode at 195.6 cm^{-1}. Once more, the discrepancy between the Raman and IR measured modes is too large to be accounted by experimental error bars.

Prior to fully exclude the $Pmn2_1$ group, we will have a look at the results in the *Pm* group, since recent single crystal x-ray diffraction yielded *Pm* to be the actual space group in the low temperature magnetic phase [14].

Table 5. Measured and computed phonon modes. The spin-polarized DFT calculations were carried out in the $Pmn2_1$ space group. The Raman modes were taken from [9] (measurements at 300 K). The IR modes were taken from our measurements at 300 K.

DFT Irrep	$Pmn2_1$	Raman [9]	IR 300 K	
	ν	300 K	$e//\mathbf{b}$	$e//\mathbf{c}$
A2	24.5			
B1	25.9			
A1	28.5			
A1	34.8			
B1	38.3			
A1	38.9			
B2	47.9			
A2	49.2			
B1	50.9			
A2	52.5			
B1	54.7			
B2	59.2		60	
A1	60.5	59		
A2	61.2			
B2	63.1		72	
A1	66.3			
B1	68.8			
A1	69.9			
B1	72.8			
A1	80.1			76
B1	85.6			
B1	89.0			
A1	92.2	88		
B2	93.1		78	
A2	94.7			
A2	103.3			
B2	106.0		97	
A1	107.2	104.3		104
A2	108.5			
B2	109.9		—	
A1	111.2	111		
B1	111.3			
B1	113.7			
A1	114.6			
B1	125.3			
A1	128.6			
B1	137.6			
A1	144.0	137		
B2	151.3			
B1	152.5			
A2	152.9			
B1	157.1			
A1	162.2			—
A2	162.9			
B2	164.1			
B2	185.2	177	176	
A2	185.6			
B1	190.1			
A2	193.8			
B2	194.1			
A1	197.5	195.6		
B2	214.7		207	
A2	214.8			
B2	216.3	222.8		

(*continued on next page*)

Table 5. Continued

DFT Irrep	$Pmn2_1$	Raman [9]	IR 300 K	
	ν	300 K	$e//\mathbf{b}$	$e//\mathbf{c}$
A2	217.1			
A1	225.1			222
B2	229.1		236	
B1	231.2			
A2	232.1			
A1	244.6			246
B1	244.8			
B1	263.9			
A1	265.4	267		
B1	283.3			
A1	285.1	280		
A1	288.8			
B1	290.7			
A1	295.4	290		
B1	299.4			

Table 6. Measured (300 K) IR phonon modes (cm^{-1}) that could not be assigned to computed ones in the $Pmn2_1$ space group.

Irrep	Raman [9]	IR 300 K	
	300 K	$e//\mathbf{b}$	$e//\mathbf{c}$
B_2		78	
A_1			94
A_1			208

4.4. The Pm group

The 69 optical phonon modes of the Pm space group are distributed into the following irreps

$$42\,\mathrm{A} \oplus 27\,\mathrm{B}$$

All modes are active in Raman and IR.

The table displaying the computed phonons modes, as well as their best assignment to our IR measurements at 10 K, and to the measured 20 K Raman modes from reference [9], is provided in supplementary material. Similar to the $Pmn2_1$ case, all Raman modes can be easily assigned. This is also the case for the IR modes when the field is along the $\vec{b}$ direction. The respective average errors for the Raman and IR $e//\vec{b}$ are respectively weaker than 5 cm^{-1} and 6.4 cm^{-1}.

Most of the IR modes with the field along $\vec{c}$ can also be assigned with small errors. However, as for the $Pmn2_1$ group, the two most intense modes (at 211 cm^{-1} and 226 cm^{-1}) cannot be properly assigned. Indeed, the only possibility for the mode at 211 cm^{-1} would be to assign it to the same computed mode as the mode seen at 200 cm^{-1} in Raman scattering. However a 18 cm^{-1} frequency difference between Raman and IR measurements seems quite unlikely. Regarding the mode at 226 cm^{-1}, it seems impossible to assign it without a significant error (23 cm^{-1}), as there are no computed modes of the proper symmetry in this energy range.

Looking at the displacement vectors associated with the phonons modes in the 200–300 cm^{-1} range, we see that they are dominated by Fe atoms displacements. As reported in the literature, neutron pair-distribution functions clearly show a large magneto-elastic coupling, with Fe atoms displacements at the onset of the AFM order [10]. In fact, while the long-range order takes place between 200 K and 255 K according to the authors, short-range magnetic correlations (with a correlation length of $\xi \sim 35$Å) are observed from neutrons diffuse scattering [10], even at room temperature.

As a consequence one may think that, in $BaFe_2Se_3$ the magnetic order could have a strong effect on the lattice dynamics. At this point let us remember that $BaFe_2Se_3$ belongs the the superconducting pnictide family and that charge, spin, and lattice degrees of freedom are strongly entangled in iron superconductors [27, 28]. Even-though $BaFe_2Se_3$ is only superconducting under pressure and at low temperature, the possibility of a spin-lattice coupling stronger than first expected need to be investigated. Indeed, growing number of works have recently accessed the importance of spin-lattice coupling in strongly correlated systems [29–31].

4.5. Importance of in-ladder magnetic order

The magnetic propagation vector in the $BaFe_2Se_3$ system is $(1/2, 1/2, 1/2)$. Computing lattice dynamics using the published [7–10] magnetic order would thus require to use a supercell of eight unit cells. As stated before, unfortunately, such a large calculation is beyond our present possibilities. The magnetic structure is however highly anisotropic, with much larger magnetic couplings within the ladders than between them. One can thus expect that (1) it is the intra-ladder magnetic order that is responsible for the magneto-lattice coupling, and (2) that this effect may also be present in the paramagnetic phase. We therefore recomputed the phonons modes, both in the Pm and $Pmn2_1$ groups, using a double super-cell ($\vec{a} \times 2\vec{b} \times \vec{c}$), and spin-polarized calculations with the experimental spin ordering along the ladders direction ($\vec{b}$).

The first consequence was, as expected, a large energy stabilization (16.831 eV for the $Pmn2_1$ group and 16.833 eV

Table 7. Spin-polarized calculation of $BaFe_2Se_3$ phonon modes in the *Pm* group and their best assignment to the experimental Raman [9] and infrared modes. Modes with stars are estimated graphically, thus they should be taken with caution.

DFT Irrep	*Pm*	Raman [9]		IR 300 K		IR 10 K	
	ν	300 K	20 K	$e//\mathbf{b}$	$e//\mathbf{c}$	$e//\mathbf{b}$	$e//\mathbf{c}$
B	24.2						
A	26.2						
A	28.7						
A	34.9						
A	38.5						
A	39.2						
B	49.0						
B	49.7						
A	51.1						
B	53.5						
A	54.6						
B	59.7			60		61	
A	60.6	59	63.4				
B	64.0			72		75	
A	66.3						
B	67.7			78		79	
A	69.0						
A	70.1						
A	72.9						
A	79.9				76		79
A	85.8						
A	89.3	88	89				
A	92.3				94		96
B	93.1						
B	94.8						
B	105.0			97		105	
B	106.2						
B	106.7						
A	107.3	104.3	108	104		108	
B	108.8			—		116	
A	111.4						
A	111.4						
A	113.7						
A	114.6	111	115				
A	125.2						
A	128.4						
A	137.6						
A	143.9	137	143				
B	151.4						
A	152.5						
B	152.8						
A	157.0						
A	162.1				—		163
B	164.1						
B	165.3						
B	176.3	177	183.8	176		179	
B	185.7						
B	186.5						
B	188.8		198				
A	190.3						
A	197.5	195.6	200				
B	210.2			207^*		210^*	
B	211.9						
B	216.0						
B	217.1						

(*continued on next page*)

Table 7. Continued

DFT Irrep	*Pm*	Raman [9]		IR 300 K		IR 10 K	
	ν	300 K	20 K	$e//\mathbf{b}$	$e//\mathbf{c}$	$e//\mathbf{b}$	$e//\mathbf{c}$
A	225.6				208		211
B	230.7	222.8	228				
A	231.2				222		226
B	232.9			236		241	
A	245.0						
A	245.3				246		248
A	264.3						
A	265.6	267	272				
A	283.7	280	288.7				
A	285.6						
A	288.9						
A	291.0						
A	295.6	290	296.5				
A	299.5						

for the *Pm* group) compared to the non spin-polarized calculations. The energy difference between the $Pmn2_1$ and *Pm* groups remains, however, non significant (∼3 meV). Looking at the geometries, one sees that the spin-polarized optimized geometries differ from the non spin-polarized ones, as far as the Fe–Fe distances along the ladders are concerned.

The non spin-polarized geometries are all similar to the *Pnma* experimental one. Indeed, in all of them we find alternated trapezoidal blocks, as a result of the Fe–Fe distances alternation along the ladders (see figure 6(a)). In contrast to this, the spin-polarized optimized geometries present an alternation between small and large rectangular blocks (see figure 6(b)), as in the experimental $Pmn2_1$ and *Pm* structures [14].

This feature originates from the spin-ordering along the ladders. This can be checked by re-optimizing the geometry within a non spin-polarized calculation, starting from the spin-polarized one. In such calculations the resulting bond lengths exhibit again trapezoidal blocks (figure 6(a)).

Tables 5 and 6 report the spin-polarized phonons calculations at the Γ point, in the $Pmn2_1$ group. As we worked in a double unit cell, CRYSTAL provides both the Γ point and zone-border M-point phonons. We thus wrote a small code to identify the former, as well as their irrep. For this purpose, we used the usual group-symmetry projection operator on an irrep (i)

$$P_{(i)} = \frac{1}{|G|}\sum_{g\in G}\chi^*_{(i)}(g)\ g,$$

where $|G|$ is the order of the group G, g any symmetry operation belonging to G and χ the characters. In the following tables we will only present the Γ point phonons, as they are the only ones seen in Raman or IR measurements.

As can be seen, there still are three IR phonons modes that cannot be assigned with the computed frequencies. The B_2 mode at 78 cm^{-1} and the A_1 modes at 94 cm^{-1} and 208 cm^{-1}. In fact, the two A_1 modes could be assigned to computed ones with reasonable errors. However, as previously, there are Raman modes already associated with these frequencies (namely at 88 cm^{-1} and 196 cm^{-1}) and the differences between the experimental modes are too large to be accounted for experimental error bars. The $Pmn2_1$ space group is thus unlikely to be $BaFe_2Se_3$ space group, even at 300 K.

Let us now check the *Pm* group. Table 7 report spin-polarized phonons calculations at the Γ point, in the *Pm* group.

As can be seen in table 7 all experimental Raman and IR modes can now be easily assigned to the theoretical ones. The average error on the Raman modes at 20 K and 300 K is smaller than 4 cm^{-1}, while it is smaller than 6 cm^{-1} for the IR modes measured at 300 K and 5 cm^{-1} for the IR modes measured at 10 K. From these results one can thus confirm that the space group of $BaFe_2Se_3$ is *Pm* in the magnetic phase, and infer it should also be *Pm* and not $Pmn2_1$ or *Pnma* at 300 K, in the paramagnetic phase.

5. Conclusion

In the present paper we report a combined experimental and theoretical study of the lattice dynamics in $BaFe_2Se_3$. The comparison of our IR measurements and computed phonons frequencies in the *Pnma*, $Pmn2_1$ and *Pm* space groups shows that *Pm* is the only possible space group, not only in the low temperature magnetic phase, but also on the high temperature paramagnetic phase.

Our calculations reveals that the magnetic order within the ladders plays a crucial role, even in the paramagnetic phase. This is in agreement with neutrons diffuse scattering experiments, that support the existence of a short-range magnetic order in the paramagnetic phase, with an approximate correlation length of 35 Å [10]. In fact, both the optimized structure and the phonons modes strongly differ in some key-points, when the magnetic order along the ladders is taken into account in the calculations. The first difference resides in the Fe–Fe distances along the ladder legs. Indeed, in a non spin-polarized calculation, the Fe–Fe bond lengths along the ladders exhibit a short/long long/short trapezoidal pattern (see figure 6(a)); whereas in a spin-polarized calculation, the spin-ordering along the ladders induces a complete change of the Fe–Fe bond lengths pattern, with an alternation of large and small rectangular blocks (see figure 6(b)). The latter blocks pattern is in good agreement with our x-ray diffraction measurements of reference [14], while the trapezoidal pattern is in good agreement with the *Pnma* x-ray structure from reference [10]. It is also of crucial importance to note that the rectangular blocks pattern is fully compatible with the block AFM structure, while the trapezoidal pattern is not. Indeed, if the short/long Fe–Fe bonds are associated to AFM/FM exchange integrals, the experimental magnetic ordering seen along the ladders becomes obvious. The determination of the magnetic integrals associated with the *Pm* structure should thus be our next piece of work. This resolves the puzzle of the crystal structure incompatibility with the magnetic structure, often discussed in the literature.

At 660 K $BaFe_2Se_3$ undergoes a *Cmcm* to *Pnma* phase transition [32], followed by another transition at 425 K. The latter transition was shown, by scanning transmission electron microscopy, to be associated with an in-ladder tetramerisation, a differentiation between the two ladders of the unit cell and a room temperature polarization [16]. Putting these experimental results into perspective with our lattice dynamic study, one can built a coherent picture for the $BaFe_2Se_3$ phase diagram. After the 660 K phase transition from the *Cmcm* group to *Pnma*, the 425 K phase transition can be associated to a *Pnma* to *Pm* symmetry lowering, induced by the inset of the short-range magnetic correlations within the ladders. Such a transition would be in agreement with the inset of the tetramerisation, the polarization and the release of the symmetry relationship between the two ladders. It would also account for the observed strong coupling between the lattice and the short-range magnetic order.

Acknowledgments

The theoreticians among the authors thank the IDRIS (Project No. 91842) and CRIANN (Project No. 2007013) computer centers on which the calculations presented in this paper have been done. They were also supported by the French National Research Agency in the framework of the 'Investissements d'avenir' program (ANR-15-IDEX-02). The experimental work was financially supported by the ANR COCOM 20-CE30-0029 and by the CSC scholarship (No. 201806830111). We also thank SOLEIL for synchrotron beam time (Proposal 20211300).

Data availability statement

All data that support the findings of this study are included within the article (and any supplementary files).

ORCID iDs

V Balédent https://orcid.org/0000-0002-9437-434X
M-B Lepetit https://orcid.org/0000-0001-8730-4282

References

[1] Bednorz J G and Müller K A 1986 *Z. Phys.* B **64** 189
[2] Gao L, Xue Y Y, Chen F, Xiong Q, Meng R L, Ramirez D, Chu C W, Eggert J H and Mao H K 1994 *Phys. Rev.* B **50** 4260–3
[3] Schilling A, Cantoni M, Guo J D and Ott H R 1993 *Nature* **363** 56–8
[4] Takahashi H, Igawa K, Arii K, Kamihara Y, Hirano M and Hosono H 2008 *Nature* **453** 376–8
[5] Kamihara Y, Hiramatsu H, Hirano M, Kawamura R, Yanagi H, Kamiya T and Hosono H 2006 *J. Am. Chem. Soc.* **128** 10012–3
[6] Zhang Y, Zhang H, Weng Y, Lin L, Yao X and Dong S 2016 *Phys. Status Solidi RRL* **10** 757
[7] Liu X, Ma C, Hou C, Chen Q, Sinclair R, Zhou H, Yin Y and Li X 2019 *Europhys. Lett.* **126** 27005
[8] Krzton-Maziopa A, Pomjakushina E, Pomjakushin V, Sheptyakov D, Chernyshov D, Svitlyk V and Conder K 2012 *J. Phys.: Condens. Matter* **24** 059502
[9] Popović Z V, Šćepanović M, Lazarević N, Opačić M, Radonjić M M, Tanasković D, Lei H and Petrovic C 2015 *Phys. Rev.* B **91** 064303
[10] Caron J M, Neilson J R, Miller D C, Llobet A and McQueen T M 2011 *Phys. Rev.* B **84** 180409
[11] Gao J, Teng Y, Liu W, Chen S, Tong W, Li M, Zhao X and Liu X 2017 *RSC Adv.* **7** 30433–8
[12] Takahashi H *et al* 2015 *Nat. Mater.* **14** 1008
[13] Dong S, Liu J M and Dagotto E 2014 *Phys. Rev. Lett.* **113** 187204
[14] Zheng W *et al* 2020 *Phys. Rev.* B **101** 020101
[15] Nambu Y *et al* 2012 *Phys. Rev.* B **85** 064413
[16] Du K *et al* 2020 *npj Quantum Mater.* **5** 49
[17] Roy P, Rouzières M, Qi Z and Chubar O 2006 *Infrared Phys. Technol.* **49** 139–46 The AILES infrared beamline on the third generation synchrotron radiation facility SOLEIL https://doi.org/10.1016/j.infrared.2006.01.015
[18] Dovesi R *et al* 2018 *WIREs Comput. Mol. Sci.* **8** e1360
[19] Dovesi R *et al* 2017 *Crystal17 user's manual* (Torino: University of Torino)
[20] Aroyo M I 2016 *Vol. A, Space-Group Symmetry* (New York: Wiley)
[21] Becke A D 1993 *J. Chem. Phys.* **98** 5648–52
[22] Stephens P J, Devlin F J, Chabalowski C F and Frisch M J 1994 *J. Phys. Chem.* **98** 11623–7
[23] Heyd J, Peralta J E, Scuseria G E and Martin R L 2005 *J. Chem. Phys.* **123** 174101
[24] Kaupp M, Schleyer P V R, Stoll H and Preuss H 1991 *J. Chem. Phys.* **94** 1360–6
[25] Orobengoa D, Capillas C, Aroyo M I and Perez-Mato J M 2009 *J. Appl. Crystallogr.* **42** 820–33
[26] Perez-Mato J M, Orobengoa D and Aroyo M I 2010 *Acta Crystallogr.* A **66** 558–90
[27] Chauvière L, Gallais Y, Cazayous M, Méasson M A, Sacuto A, Colson D and Forget A 2011 *Phys. Rev.* B **84** 104508
[28] García-Martínez N A, Valenzuela B, Ciuchi S, Cappelluti E, Calderón M J and Bascones E 2013 *Phys. Rev.* B **88** 165106
[29] Poojitha B, Rathore A, Kumar A and Saha S 2020 *Phys. Rev.* B **102** 134436
[30] Bansal D *et al* 2020 *Nat. Phys.* **16** 669–75
[31] Bajaj N *et al* 2021 *J. Phys.: Condens. Matter* **33** 125702
[32] Svitlyk V, Chernyshov D, Pomjakushina E, Krzton-Maziopa A, Conder K, Pomjakushin V, Pöttgen R and Dmitriev V 2013 *J. Phys.: Condens. Matter* **25** 315403